

Article

A Computational Study on Performance Improvement of THz Signal from a Grating Photoconductive Antenna

Jia Yi Chia *, Khwanchai Tantiwanichapan, Rungroj Jintamethasawat, Asmar Sathukarn, Woraprach Kusolthossakul and Noppadon Nuntawong

National Electronics and Computer Technology Center (NECTEC), 112 Thailand Science Park, Phahonyothin Road, Khlong Nueng, Khlong Luang, Pathum Thani 12120, Thailand; khwanchai.tantiwanichapan@nectec.or.th (K.T.); rungroj.jintamethasawat@nectec.or.th (R.J.); asmar.sathukarn@nectec.or.th (A.S.); woraprach.kus@ncr.nstda.or.th (W.K.); noppadon.nuntawong@nectec.or.th (N.N.)

* Correspondence: jia.yi.chia@nectec.or.th

Received: 1 October 2020; Accepted: 26 October 2020; Published: 11 November 2020



Abstract: A diffractive grating is a well-known optical component and is extensively used in many applications. This research work explores application of the diffractive grating in a photoconductive antenna (PCA) of a terahertz time domain spectroscopy (THz-TDS) system, by utilizing benefits of a sub-wavelength grating structure. The grating PCA structure was modeled and simulated by COMSOL Multiphysics software (COMSOL, Inc., Burlington, MA, USA). Performance of the proposed PCA design is studied in terms of its induced photocurrent. The effects of geometrical parameters of the grating are also investigated and analyzed through its optical and electrical responses. Thanks to the increase in absorption of the incident laser's electric field, the simulation results show a 63% increment of the induced photocurrent in the grating PCA, compared with the conventional planar PCA.

Keywords: diffractive grating; anti-reflection; THz time domain spectroscopy; photoconductive antenna

1. Introduction

A grating is a periodic array of lines, slits, grooves, or other variations that split and diffract light into several beams travelling in different directions. One example of the natural phenomenon caused by the surface grating is the structural coloration in various animals [1,2]. However, the first manmade grating was reported in 1785 by Rittenhouse and a major breakthrough was achieved in 1821 by Fraunhofer in both fabrication and optical characterization of diffractive gratings. Since then, there have been many types of diffractive gratings designed for a wide range of applications, such as an amplitude grating, a blazed grating, an echelle grating, a lamellar grating, and an interference grating [3]. A diffractive grating is recognized as one of the essential components in the spectroscopy systems. At the same time, it is also utilized in laser systems, astronomical applications, and synchrotron radiation beamlines [4].

A subwavelength grating, also known as a surface-relief grating or an anti-reflection grating, is one kind of diffractive grating whose period is smaller than the illuminating wavelength. Unlike a typical diffractive grating, the subwavelength grating allows only the reflected and transmitted zeroth-order modes to propagate, while higher diffraction orders are evanescent [5,6]. Besides being birefringent, the optical properties, including its refractive index, of a subwavelength grating could be engineered by varying grating parameters [7,8]. As a result, these grating were used as an anti-reflection surface, a polarization-selective device, and a guided-mode resonance filter [9]. Recently, one of the applications

of the subwavelength grating is to improve the efficiency of photovoltaic devices, such as solar cell [10–12]. In this work, we explore a new application of an anti-reflective subwavelength grating by incorporating its structure in a photoconductive antenna (PCA) of a terahertz time domain spectroscopy (THz-TDS) system.

A PCA is an optoelectronic device which could be employed as both emitter and detector in a THz-TDS system [13]. Their components and functions are shown in Figure 1. The PCAs based THz-TDS system has an advantage of being able to operate at room temperature, while still achieving a coherent detection. These allow us to obtain broadband, high signal-to-noise ratio (SNR) signals containing both amplitude and phase information. While THz-TDS systems serve as potential equipment for future research and applications [14], the main drawback of the PCA is its low optical-to-THz conversion efficiency, thus limiting the applications only in examining thin or low-absorbing specimens.

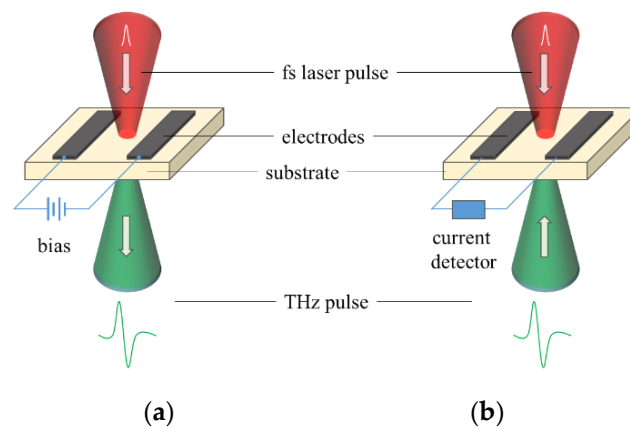


Figure 1. Schematic diagram of photoconductive antenna (PCA) as (a) an emitter and (b) a detector in a terahertz time domain spectroscopy (THz-TDS) system.

In recent decades, the significant advancement in nanotechnology has brought attention to the study of the nanostructured PCAs in order to improve their performance. Some examples are metallic nanoislands, plasmonic contact electrodes, and plasmonic nanostructures on the PCA structure [15–24]. Researchers have proved that the optical-to-THz conversion efficiency of the plasmonic based PCA greatly increases due to the local field enhancement and the reduction in thermal and carrier screening effects [25,26]. Another approach in improving the PCA output power is by depositing an anti-reflection coating, such as silicon nitride, titanium oxide, aluminum oxide, and zinc oxide nanorods, on the PCA surface [27–31]. By estimation, a PCA on GaAs substrate with a perfect anti-reflection surface can totally suppress Fresnel reflection thus result in a 48% higher absorption and consequently enhance the THz power. Similarly, the anti-reflection effect of a PCA could be achieved by incorporating a grating structure into the photoconductive substrate. Compared to the anti-reflection coatings, a subwavelength grating has an advantage as the spatial distribution of the electric field could be optimized by engineering its geometrical parameters. Furthermore, it could also avoid the adhesion problem and other limitations induced from the exotic coating materials.

In this work, a new design of PCA consisting of the antenna electrodes deposited on a subwavelength grating low-temperature grown GaAs (LT-GaAs) substrate is proposed. The optical induced photocurrent of the proposed structure is simulated by using COMSOL Multiphysics, a commercially available finite element method (FEM) solver. The geometrical parameters of a grating PCA, such as period (Λ), filling factor (F), and depth (D), were varied and investigated through their electrical and optical responses. Based on the simulation results, this new design would improve the optical-to-THz efficiency up to 63%, compared to a conventional PCA. Besides, the proposed design also has an advantage in terms of fabrication as the fabrication techniques of both grating and antenna electrodes are already well-explored and formulated. In this article, Section 2 explains the theory

supporting this work, Section 3 shows the developed simulation model, Section 4 discusses the results, and conclusions of the work is given in Section 5.

2. Theory

The effective medium theory (EMT) is applied to describe the interaction of light with a subwavelength grating as the grating structure (as illustrated in Figure 2) can be well approximated as a homogeneous uniaxial layer posing an effective refractive index, n_{eff} [32,33]. The effective index is affected by the grating parameters, the polarization of the incident light, and the refractive index of the surrounding medium. If polarization is not taken into account, n_{eff} of the grating structure is represented by

$$n_{eff} = n_1 + F \cdot (n_2 - n_1), \tag{1}$$

where n_1 and n_2 are the refractive indices of the surrounding medium and the grating material, respectively. The filling factor, $F = W/\Lambda$, represents the volume fraction of the material with index n_2 whereas W and Λ are the grating slab width and the grating period, respectively.

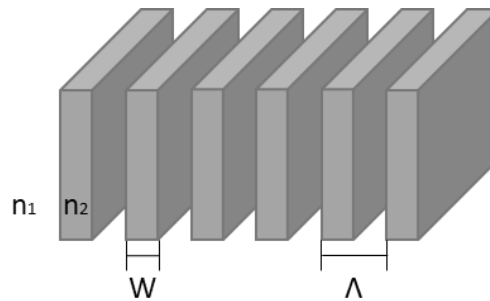


Figure 2. The grating structure and the parameters used in calculating the effective refractive index, n_{eff} . The grating slabs are illustrated by the gray blocks.

Equations (2) and (3) are used in estimating the n_{eff} of the grating in the case where the incident light is polarized.

$$n_{eff,\parallel} = [(1 - F) \cdot n_1^2 + F \cdot n_2^2]^{1/2}, \tag{2}$$

$$n_{eff,\perp} = [(1 - F) \cdot n_1^{-2} + F \cdot n_2^{-2}]^{-1/2}, \tag{3}$$

where $n_{eff,\parallel}$ and $n_{eff,\perp}$ are the effective indices where the incident electric field vector is parallel and perpendicular to the grating slabs, respectively.

The following mathematical equations describe how the PCA performs. First, the electric field distribution in the simulation entity can be described and derived (in frequency domain) from Maxwell's equations:

$$\nabla \times \mu_r^{-1} (\nabla \times \mathbf{E}) - k_0^2 (\epsilon_r - j\sigma/(\omega\epsilon_0)) \mathbf{E} = 0, \tag{4}$$

where \mathbf{E} is the complex electric field vector. μ_r , ϵ_r , and σ are the relative magnetic permeability, electrical permittivity, and electrical conductivity of the material, respectively. k_0 , ϵ_0 , and ω are the free-space propagation constant, the free-space permittivity, and the angular frequency of the incident wave, respectively. Note that ϵ_r and σ are based on Drude-Lorentz model, which includes the interband transition with Lorentz oscillation.

The incident electric field (4) with the total power P is absorbed by the substrate and then free carriers are generated. Assuming that the laser has a Gaussian shape in a temporal dimension, the generation rate R_{GEN} can be defined as the following proportionality relation:

$$R_{GEN}(x,y,z,t) \propto P \cdot \alpha(x,y,z) \cdot \exp(-(t - t_c)^2/(w_t^2)) \cdot (hf - E_g)^{1/2}, \tag{5}$$

where α is the spatially-dependent effective photon absorption coefficient of the substrate, t_c is the center of the Gaussian peak, w_t is the Gaussian width of the laser pulse, h is Planck's constant, f is the incident frequency, and E_g is the bandgap of the semiconductor substrate.

Although the laser illumination is uniform across the substrate, this does not imply that the generation rate is also constant due to the structure of the substrate. The refractive index mismatch between the substrate and air could cause the absorption and reflection of the incident electric field, which could change the electric field power and generation rate subsequently.

Once free carriers are generated, they will move along the direction of the bias electric field. The carrier dynamics can be solved by using Poisson's Equation (6) and the continuity equations for electrons and holes, in time domain (7) and (8).

$$\nabla \cdot (\epsilon_r \nabla V) = q(n - p + N_A - N_D), \quad (6)$$

$$\partial n / \partial t = 1/q \nabla \cdot \mathbf{J}_n + (R_{GEN} - R_{REC}), \quad (7)$$

$$\partial p / \partial t = -1/q \nabla \cdot \mathbf{J}_p + (R_{GEN} - R_{REC}), \quad (8)$$

where V represents the voltage distribution in the substrate, n and p are the electron and hole concentration, q is the electron charge, N_A and N_D are the acceptor and donor ion concentration, \mathbf{J}_n and \mathbf{J}_p are the electron and hole current density, and R_{GEN} and R_{REC} are the generation and recombination rates, respectively, of both electrons and holes. Note that these rates are the same for both electrons and holes, as the generation/recombination of one carrier will induce the same effect for the opposite charge.

The current density of electrons and holes can be calculated by the drift-diffusion equations as:

$$\mathbf{J}_n = nq\mu_n \nabla(V + V_{DC}) + qD_n \nabla n, \quad (9)$$

$$\mathbf{J}_p = pq\mu_p \nabla(V + V_{DC}) - qD_p \nabla p, \quad (10)$$

where μ_n and μ_p are electron and hole mobilities, D_n and D_p are electron and hole diffusion coefficients, and V_{DC} represents a bias voltage. When the effective mass of the hole is much larger than the effective mass of the electron (which is usually the case), electron carriers will be much more sensitive to the external stimuli including substrate structure. The THz field, E_{THz} , can be approximated from the magnitude of electron current density, $\|\mathbf{J}_n\|$, by the following relation [34]:

$$E_{THz} \propto \delta \|\mathbf{J}_n\| / \delta t. \quad (11)$$

Note that changing the substrate structure could potentially induce the change of \mathbf{J}_n which is affected by the generation rate, as seen from Equations (6)–(8). Therefore, the THz field intensity also depends on the structure of substrate.

3. Simulation Model and Methods

In this study, an FEM was applied to simulate a time-dependent current generated in a 3D grating PCA structure. In our approach, a commercial FEM-based computation tool, COMSOL Multiphysics Version 5.4 was used. The Semiconductor and Wave Optics modules were utilized and coupled to study the optical and electrical responses of a PCA. A single period of the grating PCA was modeled and solved by using periodic condition, as it would greatly reduce the computational burden. The incident laser field was specified in the Wave Optics module, and the bias voltage was defined in the Semiconductor module.

Figure 3 illustrates the proposed grating THz emitter structure and the developed simulation model. The geometrical parameters of the model are summarized in Table 1. As defined previously, F is the ratio of W to Λ . There are two materials defined in the simulation model, i.e., GaAs (blue) domains and air (transparent) domains, with their material properties imported from an existing library of the simulation software. To be specific, the intrinsic properties of GaAs were used, where μ_n

and μ_p were equal to $8500 \text{ cm}^2/\text{V}\cdot\text{s}$ and $400 \text{ cm}^2/\text{V}\cdot\text{s}$, respectively. No doping profile is added to the material; hence, N_A and N_D are equal to zero. To ensure numerical stability, the coarsest mesh was set as 6 elements per GaAs refractive index per wavelength.

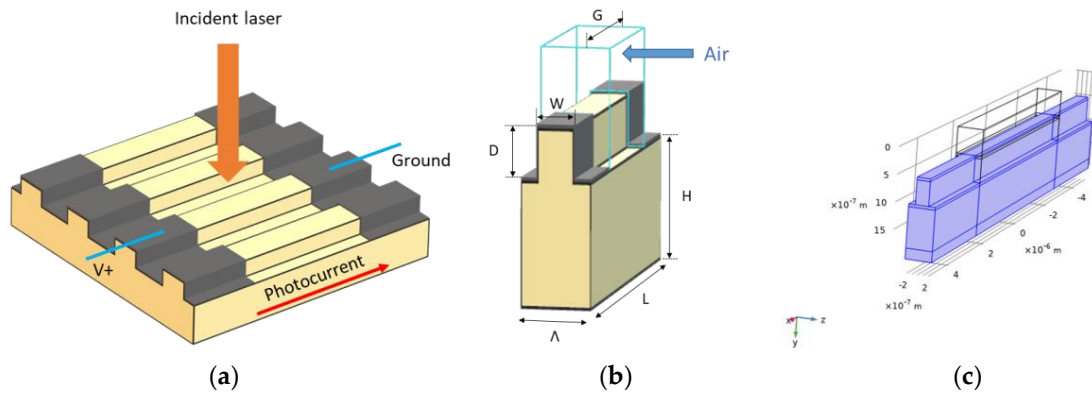


Figure 3. The schematic diagram of (a) the proposed periodic grating PCA and (b) a reduced structure for simulation purposes. Yellow color represents the photoconductive substrate, LT-GaAs, while gray color illustrates the electrodes of PCA. (c) The developed simulation model captured from the COMSOL Multiphysics Version 5.4 software.

Table 1. The geometrical parameters of the grating PCA.

Parameter	Value
Grating period, Λ	$0.5 \mu\text{m}$
Grating depth, D	$0.5 \mu\text{m}$
Filling factor, F	0.5
Substrate height, H	$1 \mu\text{m}$
Substrate length, L	$10 \mu\text{m}$
Photoconductive gap, G	$5 \mu\text{m}$

The incident wave was defined as a periodic port at the air surface with a wavelength of 780 nm , a peak power of 10 mW , and a Gaussian time profile of 100 fs pulse width with 300 fs delay time. In the port setting, the electric field mode was selected, and the incident wave was set to be perpendicular to the grating groove by enabling only the z -component of the electric field, E_z . A continuity periodic condition was set for the side walls of the grating in parallel with the x -axis to make the electric field equal on both the source and destination boundaries. This was done to simulate the behaviors of other grating periods without significantly increasing computation. The antenna was defined as two ideal ohmic contacts with a bias voltage of 20 V . A Shockley-Read-Hall (SRH) model trap-assisted recombination with an ultrashort lifetime of 1 ps was added to imitate the well-known material behavior of PCA, LT-GaAs. The Optical Transitions node in the interface configured the coupling between two interfaces to compute the carrier generation and recombination rates.

By using a frequency-transient study in time domain, the photocurrent generated in grating PCA model was computed in a range of 5 ps with a time step of 20 fs . In order to observe the grating effect, the absorbance, reflectance, and transmittance were measured at the port on top and bottom of the designed PCA. A conventional planar PCA was modeled by setting F to 1 and compared with the proposed grating PCA structure. The parametric study of the grating PCA was carried out by varying Λ , D , and F . Note that only one parameter was varied at a time, while the other two were fixed.

4. Result and Discussion

The THz signal generated by a PCA emitter is indirectly observed via induced photocurrent from a simulation as mentioned earlier in this study. Figure 4 shows the computational results of the

simulated grating and planar PCA models. For both PCAs, the magnitude of electric field (i.e., norm) of a 780 nm-incident pulse, probed at the center of excitation port, shows a maximum amplitude of approximately 2 MV/m with a peak position at 300 fs. The induced transient photocurrent drastically increases at a rate approximately proportional to the optical pulse and decreases afterward by the effects of trap-assisted recombination. In both PCAs, there is no significant difference in the pulse width of the photocurrent as it is determined by the recombination lifetime and the photoconductive gap between the electrodes. Based on simulation results, the calculated peak photocurrent of the grating PCA is 25.75 μA , which is approximately 50% larger than that of the planar PCA (peaked at 17.19 μA).

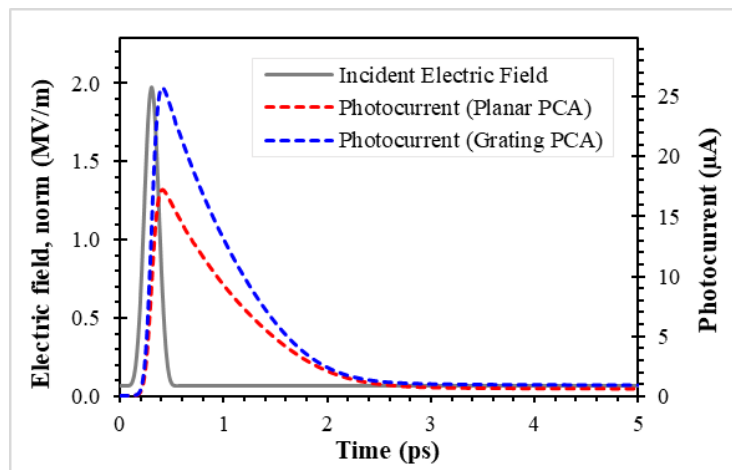


Figure 4. The probed electric field norm at the center of the excitation port (solid gray) and the induced currents generated at the terminal of the planar (dashed blue) and grating (dashed red) PCAs.

The enhancement of the induced photocurrent is explained through the increase in generated carrier concentration, n , in the grating PCA. Figure 5 shows the normalized total free electron carriers in both PCA models with respect to time. Observe that their rise times are similar: the peak amplitudes are located at approximately $t = 400$ fs, which is shortly after the peak amplitude of incident wave. This is due to the same photocarrier generation time in both PCAs. Figure 5 suggests that the grating PCA yields 32% more free electron carriers compared to that of the planar PCA. By comparing Figure 5 to the photocurrent in Figure 4, the decay of the photocurrent appears to correspond to the changes in n .

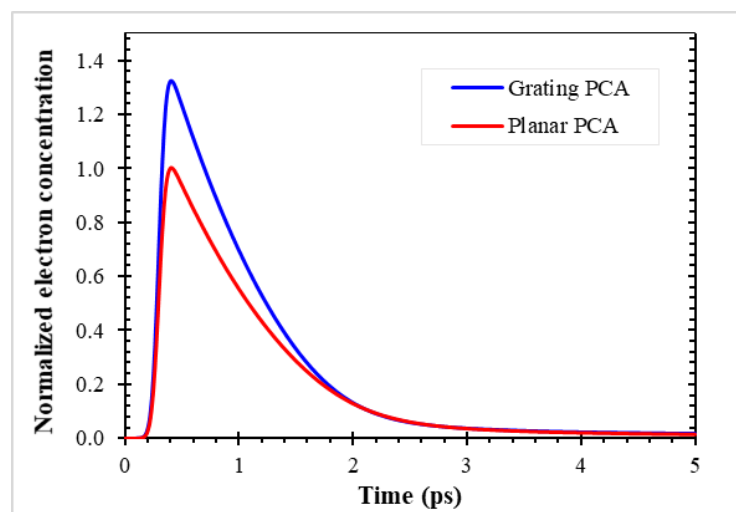


Figure 5. The temporal behavior of the normalized total number of electron carrier observed in the grating PCA (blue) and planar PCA (red).

As explained in Section 2, the electrical responses of the PCA are results from its optical response. The optical response of the simulated PCA is illustrated by the electric field distribution in the model. Figure 6 shows the spatial distribution of the z component of the electric field, E_z , in the planar and the grating PCA models. For both structures, a higher magnitude of E_z is found in the air domains compared to the substrate. Unlike the planar PCA, a diffraction pattern appears in the grating structure. Based on the results, a higher intensity of E_z with a maximum magnitude around 1.69 MV/m is found in the grating PCA substrate, compared to the planar PCA. The maximum magnitude of E_z in the planar PCA is 0.74 MV/m. The results indicate that the planar PCA has a lower optical absorbance, despite its larger active area.

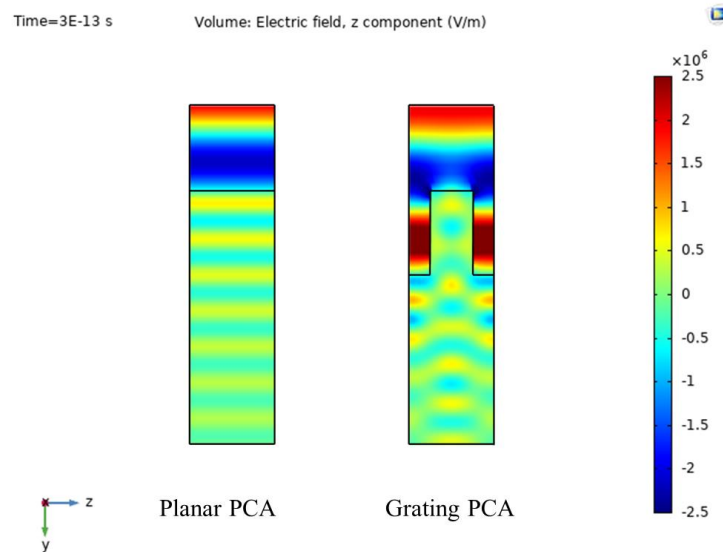


Figure 6. The z component of the electric field of a planar PCA and a grating PCA at a peak excitation time point, $t = 300$ fs. The geometrical parameters listed in Table 1 apply to both grating and planar PCAs, except $F = 1$, which is used for the planar PCA.

The grating PCA yields a higher photocurrent compared to the planar PCA because of their corresponding absorbance. Here, the optical property of a grating structure is investigated. The absorption in LT-GaAs and the reflection at the interface can be explained by the following Fresnel’s reflection equation:

$$R = [(n_2 - n_1)/(n_2 + n_1)]^2, \tag{12}$$

$$A = 1 - R, \tag{13}$$

where A is the absorbance, and R is the reflectance at the interface. By substituting $n_1 = 1$ (air) and $n_2 = 3.685$ (LT-GaAs at 780 nm), the reflectance and absorbance of a planar PCA are 0.328 and 0.672, respectively. By using Equation (3), where the electric field is perpendicular to the grating slabs, $n_{eff,\perp}$ of a grating PCA is equal to 1.3648 for a grating structure with $F = 0.5$ (as shown in Figure 7). Note that the values of n_1 and n_2 used in the calculation are the same as those in COMSOL simulation model, however only the real part of the refractive index is used in the calculation. Table 2 lists the reflectance and absorbance obtained by a calculation and a simulation. Both results show that the grating PCA has a smaller reflectance and a larger absorbance than those of the planar PCA. These results confirm a higher laser absorbance due to the anti-reflection effect from n_{eff} in the grating structure.

The effects of Λ in the grating PCA are investigated by varying the value of Λ from 0.25 μm to 2.0 μm . To ensure the same peak intensity applied, for all cases, the power of the incident laser is normalized by the area of the air domain, i.e., a larger Λ structure is excited with a higher laser power. Figure 8 represents the induced photocurrent per laser illuminating area in the grating PCAs and the corresponding planar structures. Apparently, the photocurrent of a planar PCA is not influenced by the

parameter Λ . As such, the value of photocurrent per area is ranging from 6.85 A/mm² to 6.88 A/mm². Based on the simulation, the resulting photocurrent of a grating PCA is always higher than that of the planar PCA. Contrary to the planar PCA, Λ greatly affects the THz output signal of a grating PCA, especially the cases of Λ smaller than the incident laser wavelength. The increment factor is defined as a ratio of the induced photocurrent in the grating PCA to that of the planar PCA. For the cases of $\Lambda \leq 780$ nm, the increment factor is ranging from 1.43 to 1.63. The increment factor when $\Lambda > 780$ nm is ranging from 1.18 to 1.31. This indicates that a smaller Λ structure can better enhance the THz emission of a PCA.

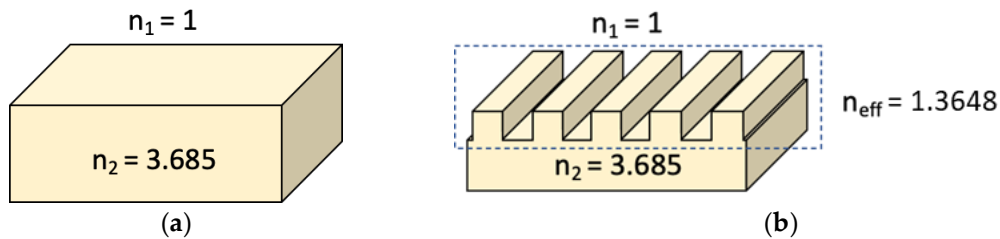


Figure 7. The refractive index of (a) the planar PCA and (b) the grating PCA structures used for Fresnel’s reflection calculation.

Table 2. The optical properties of a grating PCA and a planar PCA.

Structure	Reflectance		Absorbance	
	Simulation	Calculation	Simulation	Calculation
Planar PCA	0.329	0.328	0.615	0.672
Grating PCA	0.029	0.230	0.851	0.770

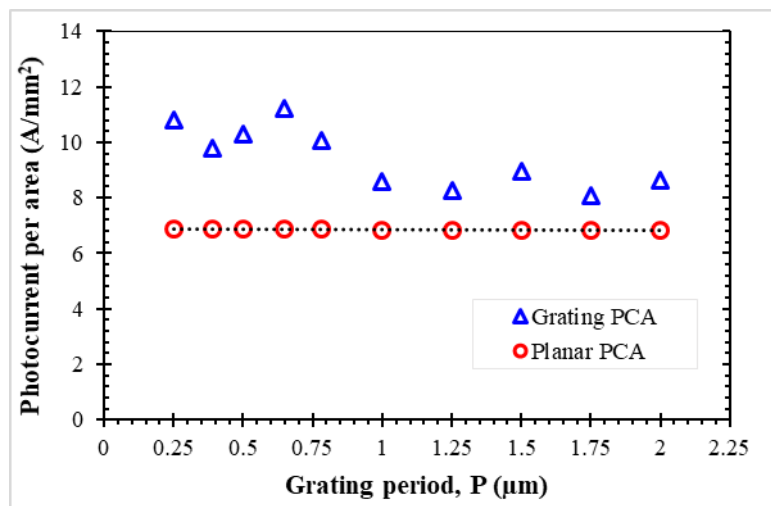


Figure 8. The simulated photocurrent in the planar PCA (red circle) and grating PCA (blue triangle) against grating period Λ . The planar PCA refers to $F = 1$ (done by setting $W = \Lambda$). For the planar PCA, the induced photocurrent per illuminating area is almost constant.

Next, the effects of parameter F in a $\Lambda = 0.5$ μm grating PCA are investigated by varying F in Table 1, from 0.1 to 0.9, with a step size of 0.1. Cases of $F = 0$ and $F = 1$ are the planar PCA with a substrate thickness of 1.0 μm and 1.5 μm , respectively. Figure 9 shows the photocurrent and the optical absorbance of the grating PCA with all values of F . The simulation results show that the case of $F = 0.5$ exhibits the best absorbance of 0.851 of the incident wave. The optical absorbance of 0.831 at $F = 0.7$ is slightly less than that at $F = 0.5$, and it has the highest photocurrent among all studied cases, 27.46 μA .

Compared to the planar PCA ($F = 1$), all the grating PCAs, except at $F = 0.1$, exhibit a significantly better absorbance and, thus, photocurrent, with the increment factors of 1.37 to 1.60.

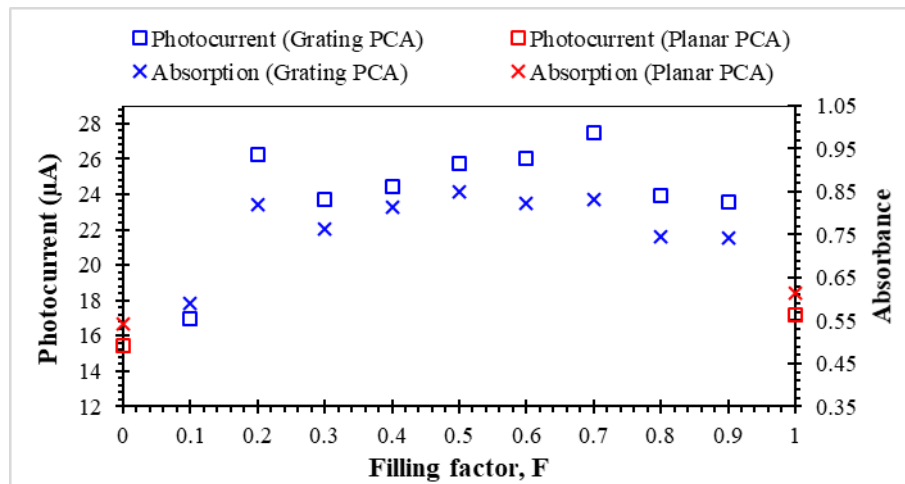


Figure 9. The photocurrent in the grating PCA (blue square) and the planar PCA (red square) with various F and their corresponding optical absorbance (blue cross for grating PCA and red cross for planar PCA). Note that the case of $F = 0$ corresponds to the planar PCA with a thickness of H , while $F = 1$ refers to the planar PCA with a total thickness of $H + D$.

The last parameter of our interest, D , is studied for the grating structure by varying D in Table 1, from $0 \mu\text{m}$ to $0.7 \mu\text{m}$, where $0 \mu\text{m}$ is the planar PCA with a thickness of H only. Note that $\Lambda = 0.5 \mu\text{m}$ and $F = 0.5$ are used here. According to Figure 10, for the planar PCA, the photocurrent tends to increase with respect to the increase of the LT-GaAs substrate thickness. This increment becomes less significant when D is large enough. For example, there is only $0.007 \mu\text{A}$ difference between $D = 0.6 \mu\text{m}$ and $D = 0.7 \mu\text{m}$, whereas there is $0.59 \mu\text{A}$ difference between $D = 0 \mu\text{m}$ and $D = 0.1 \mu\text{m}$. For the grating PCA, there is always an apparent improvement in the induced current compared to that of the planar PCA, especially when $D \geq 0.5 \mu\text{m}$. The increment factor for $D \geq 0.5 \mu\text{m}$ is observed to range from 1.10 to 1.50.

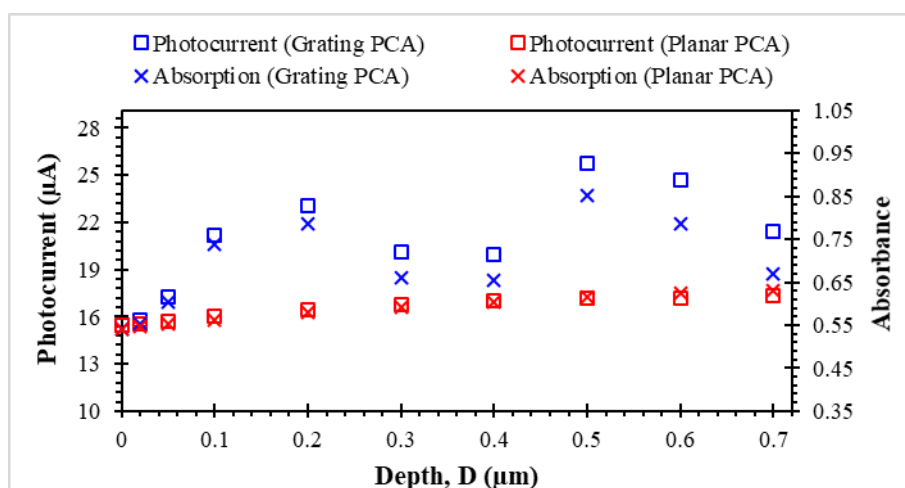


Figure 10. The photocurrent in grating PCA (blue square) and planar PCA (red square) with various D and their corresponding optical absorbance (blue cross for grating PCA and red cross for planar PCA). Note that change in D implies change in the total thickness ($D + H$).

Nonetheless, the increase in D for a grating PCA shows a non-descriptive trend in the simulated photocurrent, unlike the planar PCA. However, we can see a strong correlation between the photocurrent and the absorbance of a grating. This confirms that the increase in the photocurrent is due to the increment in the incident wave absorption. Still, the results show that the optical properties of a grating PCA are greatly influenced by the geometrical structure of grating. The earlier research work has proved that the reflected intensity of a dielectric surface-relief grating strongly depends on the groove depth [35].

5. Conclusions

By incorporating a subwavelength grating structure into a terahertz photoconductive antenna (PCA), a novel application of a diffractive grating was demonstrated. A simulation model was developed by using COMSOL Multiphysics software to investigate the optical and electrical responses of the proposed grating PCA structure. The geometrical parameters period (Λ), depth (D), and filling factor (F) of the grating PCA were varied and their effects on THz signal were investigated. The results show a 1.63 times higher photocurrent in the grating PCA compared with that in the conventional planar PCA. Combining the optical response and the electrical response, a grating PCA exhibits a higher photon absorption and leads to more carrier generation in the materials, which ultimately results in a higher photocurrent. Further experimental verification is still needed as a future work to ensure the feasibility of the proposed idea and the obtained simulation results.

Author Contributions: Conceptualization, K.T.; methodology, R.J. and A.S.; writing—Original draft preparation, J.Y.C.; writing—Review and editing, W.K. and N.N. All authors have read and agreed to the published version of the manuscript.

Funding: This research project was funded by Functional Ingredients and Food Innovation Program under National Science and Technology Development Agency, Thailand.

Acknowledgments: We would like to thank our organization for providing funds for purchasing a software license. We also thank COMSOL support team who provides us constructive ideas in building and troubleshooting the simulation model.

Conflicts of Interest: The authors declare no conflict of interest.

References

1. Kinoshita, S.; Yoshioka, S.; Miyazaki, J. Physics of structural colors. *Rep. Prog. Phys.* **2008**, *71*, 076401. [[CrossRef](#)]
2. Parker, A.R. The diversity and implications of animal structural colours. *J. Exp. Biol.* **1998**, *201*, 2343–2347. [[PubMed](#)]
3. Palmer, E.W.; Hutley, M.C.; Franks, A.; Verrill, J.F.; Gale, B. Diffraction gratings (manufacture). *Rep. Prog. Phys.* **1975**, *38*, 975. [[CrossRef](#)]
4. Palmer, C.; Loewen, E. *Diffraction Grating Handbook*, 6th ed.; Newport Corporation: Irvine, CA, USA, 2005.
5. Glytsis, E.N.; Brundrett, D.L.; Gaylord, T.K. Review of rigorous coupled-wave analysis and of homogeneous effective medium approximations for high spatial-frequency surface-relief gratings. In Proceedings of the Conference on Binary Optics, Huntsville, AL, USA, 23–25 February 1993.
6. Stork, W.; Streibl, N.; Haidner, H.; Kipfer, P. Artificial distributed-index media fabricated by zero-order gratings. *Opt. Lett.* **1991**, *16*, 1921–1923. [[CrossRef](#)]
7. Tian, H.; Cui, X.; Du, Y.; Tan, P.; Shi, G.; Zhou, Z. Broadband high reflectivity in subwavelength-grating slab waveguides. *Opt. Express* **2015**, *23*, 27174–27179. [[CrossRef](#)]
8. Schmid, J.H.; Cheben, P.; Bock, P.J.; Halir, R.; Lapointe, J.; Janz, S.; Delage, A.; Densmore, A.; Fedeli, J.M.; Hall, T.J.; et al. Refractive index engineering with subwavelength gratings in silicon microphotonic waveguides. *IEEE Photonics J.* **2011**, *3*, 597–607. [[CrossRef](#)]
9. Mait, J.N.; Prather, D.W. *Selected Papers on Subwavelength Diffractive Optics*; SPIE Milestone Series; Society of Photo Optical Washington: Bellingham, WA, USA, 2001; Volume MS166.
10. Rao, J.; Varlamov, S. Light trapping in thin film polycrystalline silicon solar cell using diffractive gratings. *Energy Procedia* **2013**, *33*, 129–136. [[CrossRef](#)]

11. Masouleh, F.F.; Das, N.; Rozati, S.M. Nano-structured gratings for improved light absorption efficiency in solar cells. *Energies* **2016**, *9*, 756. [[CrossRef](#)]
12. Chen, R.; Hu, Z.; Ye, Y.; Zhang, J.; Shi, Z.; Hua, Y. An anti-reflective 1D rectangle grating on GaAs solar cell using one-step femtosecond laser fabrication. *Opt. Lasers Eng.* **2017**, *93*, 109–113. [[CrossRef](#)]
13. Burford, N.M.; El-Shenawee, M.O. Review of terahertz photoconductive antenna technology. *Opt. Eng.* **2017**, *56*, 010901. [[CrossRef](#)]
14. Dexheimer, S.L. *Terahertz Spectroscopy: Principles and Applications*; CRC Press: Boca Raton, FL, USA, 2017.
15. Jarrahi, M. Advanced photoconductive terahertz optoelectronics based on nano-antennas and nano-plasmonic light concentrators. *IEEE Trans. Terahertz Sci. Technol.* **2015**, *5*, 391–397. [[CrossRef](#)]
16. Park, S.G.; Choi, Y.; Oh, Y.J.; Jeong, K.H. Terahertz photoconductive antenna with metal nanoislands. *Opt. Express* **2012**, *20*, 25530–25535. [[CrossRef](#)] [[PubMed](#)]
17. Berry, C.W.; Jarrahi, M. Terahertz generation using plasmonic photoconductive gratings. *New J. Phys.* **2012**, *14*, 105029. [[CrossRef](#)]
18. Berry, C.W.; Wang, N.; Hashemi, M.R.; Unlu, M.; Jarrahi, M. Significant performance enhancement in photoconductive terahertz optoelectronics by incorporating plasmonic contact electrodes. *Nat. Commun.* **2012**, *4*, 1–10. [[CrossRef](#)] [[PubMed](#)]
19. Yang, S.H.; Hashemi, M.R.; Berry, C.W.; Jarrahi, M. 7.5% Optical-to-terahertz conversion efficiency offered by photoconductive emitters with three-dimensional plasmonic contact electrodes. *IEEE Trans. Terahertz Sci. Technol.* **2014**, *4*, 575–581. [[CrossRef](#)]
20. Berry, C.W.; Hashemi, M.R.; Jarrahi, M. Generation of high power pulsed terahertz radiation using a plasmonic photoconductive emitter array with logarithmic spiral antennas. *Appl. Phys. Lett.* **2014**, *104*, 081122. [[CrossRef](#)]
21. Yardimci, N.T.; Yang, S.H.; Berry, C.W.; Jarrahi, M. High-power terahertz generation using large-area plasmonic photoconductive emitters. *IEEE Trans. Terahertz Sci. Technol.* **2015**, *5*, 223–229. [[CrossRef](#)]
22. Jooshesh, A.; Yekta, V.B.; Zhang, J.; Tiedje, T.; Darcie, T.E.; Gordon, R. Plasmon-enhanced below bandgap photoconductive terahertz generation and detection. *Nano Lett.* **2015**, *15*, 8306–8310. [[CrossRef](#)]
23. Fesharaki, F.; Jooshesh, A.; Yekta, V.B.; Mahtab, M.; Tiedje, T.; Darcie, T.E.; Gordon, R. Plasmonic antireflection coating for photoconductive terahertz generation. *ACS Photonics* **2017**, *4*, 1350–1354. [[CrossRef](#)]
24. Burford, N.M.; Evans, M.J.; El-Shenawee, M.O. Plasmonic nanodisk thin-film terahertz photoconductive antenna. *IEEE Trans. Terahertz Sci. Technol.* **2018**, *8*, 237–247. [[CrossRef](#)]
25. Lepeshov, S.; Gorodetsky, A.; Krasnok, A.; Rafailov, E.; Belov, P. Enhancement of terahertz photoconductive antenna operation by optical nanoantennas. *Laser Photonics Rev.* **2016**, *11*, 1600199. [[CrossRef](#)]
26. Yachmenev, A.E.; Lavrukhin, D.V.; Glinskiy, I.A.; Zenchenko, N.V.; Goncharov, Y.G.; Spektor, I.E.; Khabibullin, R.A.; Otsuji, T.; Ponomarev, D.S. Metallic and dielectric metasurfaces in photoconductive terahertz devices: A review. *Opt. Eng.* **2019**, *59*, 061608. [[CrossRef](#)]
27. Headley, C.; Fu, L.; Parkinson, P.; Xu, X.; Lloyd-Hughes, J.; Jagadish, C.; Johnston, M.B. Improved performance of GaAs-based terahertz emitters via surface passivation and silicon nitride encapsulation. *IEEE J. Sel. Top. Quantum Electron.* **2011**, *17*, 17–21. [[CrossRef](#)]
28. Bjarnason, J.E.; Chan, T.L.J.; Lee, A.W.M.; Brown, E.R.; Driscoll, D.C.; Hanson, M.; Gossard, A.C.; Muller, R.E. ErAs:GaAs photomixer with two-decade tunability and 12 mW peak output power. *Appl. Phys. Lett.* **2004**, *85*, 3983–3985. [[CrossRef](#)]
29. Gupta, A.; Rana, G.; Bhattacharya, A.; Singh, A.; Jain, R.; Bapat, R.D.; Duttagupta, S.P.; Prabhu, S.S. Enhanced optical-to-THz conversion efficiency of photoconductive antenna using dielectric nano-layer encapsulation. *APL Photonics* **2018**, *3*, 051706. [[CrossRef](#)]
30. Lavrukhin, D.V.; Yachmenev, A.E.; Glinskiy, I.A.; Khabibullin, R.A.; Goncharov, Y.G.; Ryzhii, M.; Otsuji, T.; Spektor, I.E.; Shur, M.; Skorobogatiy, M.; et al. Terahertz photoconductive emitter with dielectric-embedded high-aspect-ratio plasmonic grating for operation with low-power optical pumps. *AIP Adv.* **2019**, *9*, 015112. [[CrossRef](#)]
31. Bashirpour, M.; Forouzmehr, M.; Hosseiniyjad, S.E.; Kolahdouz, M.; Neshat, M. Improvement of terahertz photoconductive antenna using optical antenna Array of ZnO nanorods. *Sci. Rep.* **2019**, *9*, 1–8. [[CrossRef](#)] [[PubMed](#)]
32. Gaylord, T.K.; Baird, W.E.; Moharam, M.G. Zero-reflectivity high spatial-frequency rectangular-groove dielectric surface-relief gratings. *Appl. Opt.* **1986**, *25*, 4562–4567. [[CrossRef](#)]

33. Ono, Y.; Kimura, Y.; Ohta, Y.; Nishida, N. Antireflection effect in ultrahigh spatial-frequency holographic relief gratings. *Appl. Opt.* **1987**, *26*, 1142–1146. [[CrossRef](#)]
34. Duvillaret, L.; Garet, F.; Roux, J.F.; Coutaz, J.L. Analytical modeling and optimization of terahertz time-domain spectroscopy experiments using photoswitches as antennas. *IEEE J. Sel. Top. Quantum Electron.* **2001**, *7*, 615–623. [[CrossRef](#)]
35. Moharam, M.G.; Gaylord, T.K. Diffraction analysis of dielectric surface-relief gratings. *J. Opt. Soc. Am.* **1982**, *72*, 1385–1392. [[CrossRef](#)]

Publisher’s Note: MDPI stays neutral with regard to jurisdictional claims in published maps and institutional affiliations.



© 2020 by the authors. Licensee MDPI, Basel, Switzerland. This article is an open access article distributed under the terms and conditions of the Creative Commons Attribution (CC BY) license (<http://creativecommons.org/licenses/by/4.0/>).